porosity, provides less stiffness, and results in lower overall frequencies.

Conclusions

The modal survey test results reported herein indicate significant differences in modal frequencies and damping ratios of the forged SSME LOX inlet tee splitter vanes relative to those of the cast tees. The difference in overall frequencies is a shift upwards (for the forged tee vanes) of about 300 Hz as compared to the vane frequencies of the previously tested cast tee vanes. The damping ratio of the forged tee vanes was also found to be lower as compared to the cast tee vane damping ratios, in general.

These differences are only due to the difference in the manufacturing processes involved in forging vs casting of the same material. The photomicrographs indicate significant grain-size differences between the forging and the casting of Inconel 718, the material with which the tees are made.

References

[1]Cairns, D. S., "Toughening Mechanisms in Multiphase Materials," 31st SDM Conf. Proceeding, Long Beach, CA, 1990, pp. 38–47.

[2]Weibull, W., "Investigations into Strength Properties of Brittle Materials," Proceedings of the Royal Swedish Inst. for Engineering Research, No. 149, 1938, pp. 1–27.

[3]Craig, R. R., Jr., *Structural Dynamics—An Introduction to Computer Methods*, John Wiley & Sons, New York, 1981.

Accurate Prediction of Drag Using Euler Methods

C. P. van Dam* and K. Nikfetrat†
University of California, Davis, Davis, California 95616

Introduction

THE problem of aerodynamic design for optimal performance in flight is a very important and demanding task in the development process of an aircraft. One of the most important parameters in the aerodynamic design process is the lift-to-drag ratio L/D. This ratio governs the efficiency of an aircraft in cruising flight for a given Mach number. Thus, both the lift and the drag must be accurately predicted for given flight conditions in order to be able to maximize L/D of an aircraft by refining and improving its shape.

Presently, computational methods based on the potential-flow equations are routinely being used to design and analyze simple (e.g., a wing) as well as complex (e.g., a complete airplane) configurations. One of the main advantages of potential methods is that fully converged solutions can be obtained in less than 1 min of CPU time on current supercomputers for typical three-dimensional problems. However, methods based on the potential-flow equations do not allow for the accurate prediction of lift and drag at higher Mach numbers. In addition, the potential-flow equations do not allow for distributed vorticity fields. Thus, rotational flow regions can only be modeled through the use of singularities which must be positioned a priori. The latter constraint is especially significant for flow calculations around three-dimensional lifting configurations. In that case, the trailing vortex sheet that originates at the trailing edge of a lifting wing with attached flow must be positioned before the flowfield can be calculated. The position of the sheet has a noticeable effect on the surface pressures and, thus, on the lift and drag force generated by the configuration.[1] Specifying the position of this vortex sheet becomes especially cumbersome for a wing body or a complete airplane configuration.

Computational methods based on the Euler equations can provide a more accurate modeling of the vortical field necessary to improve the prediction of the surface pressures as well as the lift and drag. Unfortunately, recent experiences with Euler methods have been less than encouraging. In 1988, the AGARD Fluid Dynamics Panel held a Technical Status Review on CFD-based drag prediction and analysis.[2] One of the main conclusions of the meeting was that "the application for drag prediction purposes of the current generation of Euler codes, in particular in 3D, is hampered by (over)sensitivity to grid density and quality through spurious (artificial) dissipation. For 3D wings and wing-bodies with attached flow only full potential methods with or without boundary layers appear to have some success."[2] More recent Euler results obtained by Hicks et al.[3] for commercial wing and wing-body configurations also indicate that current codes may be unacceptable for design because they are not capable of predicting drag or drag increments accurately enough.

Part of the Euler drag prediction problem may stem from the use of surface pressure integration to determine the drag. For methods based on the potential-flow equations, the integration of surface pressures can give reasonable drag values if the surface grid distribution is sufficiently fine and the numerical solution is fully converged.[4] However, for Euler methods an additional problem is the inherent numerical viscosity which affects the surface pressures especially in the stagnation region near the leading edge of a wing and in the recovery region near the trailing edge. Errors in the surface pressures in these two regions will hardly affect the lift prediction, but will significantly affect the drag prediction.

The purpose of the present paper is to review several drag prediction techniques and to compare them by applying these techniques to three-dimensional Euler solutions.

Lift and Drag from Momentum Theorem

Let us analyze the lift and drag of a wing in an unbounded fluid. The wing can be placed inside a typical control volume V, where V is bounded by a singly connected surface S. The inlet and exit faces of V are normal to the freestream vector $\boldsymbol{v} = \boldsymbol{i}U_\infty$, whereas the side faces run parallel to this vector. Applying Newton's law and the Gauss theorem and limiting the problem to inviscid, steady flows while ignoring gravity forces results in the following momentum balance:

$$\int_S \{p\boldsymbol{n} + \rho\boldsymbol{v}(\boldsymbol{v}\cdot\boldsymbol{n})\}\,dS = 0 \tag{1}$$

where $\boldsymbol{n} = \boldsymbol{i}n_x + \boldsymbol{j}n_y + \boldsymbol{k}n_z$ and $\boldsymbol{v} = \boldsymbol{i}u + \boldsymbol{j}v + \boldsymbol{k}w$. In turn, Eq. (1) can be written as the sum of a near-field, a cut, and a far-field integral:

$$\int_{S_{body}} \{p\boldsymbol{n} + \rho\boldsymbol{v}(\boldsymbol{v}\cdot\boldsymbol{n})\}\,dS + \int_{S_{cut}} \{p\boldsymbol{n} + \rho\boldsymbol{v}(\boldsymbol{v}\cdot\boldsymbol{n})\}\,dS + \int_{S_{far}} \{p\boldsymbol{n} + \rho\boldsymbol{v}(\boldsymbol{v}\cdot\boldsymbol{n})\}\,dS = 0 \tag{2}$$

Presented in part as Paper 91-0338 at the AIAA 29th Aerospace Sciences Meeting, Reno, NV, Jan. 7–10, 1991; received Feb. 24, 1991; revision received May 3, 1991; accepted for publication May 3, 1991.

*Associate Professor, Department of Mechanical, Aeronautical and Materials Engineering. Member AIAA.

†Ph.D. Candidate, Department of Mechanical, Aeronautical and Materials Engineering; currently, Research Scientist, Program Development Corporation, White Plains, NY.

For Euler flows the position of the cut is arbitrary and the contribution of the second integral in Eq. (2) is zero. Surface blowing/suction is not taken into account and, thus, the second term in the first integral of Eq. (2) is zero. Then the first integral reduces to a surface pressure integral and it represents the so-called near-field approach for the calculation of the force vector $\boldsymbol{F}$. According to Eq. (2), the force vector $\boldsymbol{F}$ on the wing can also be calculated using the far-field approach, or

$$\boldsymbol{F} = i\boldsymbol{D} + j\boldsymbol{Y} + k\boldsymbol{L} = \int_{S_{body}} (p\boldsymbol{n})\, dS$$

$$= -\int_{S_{far}} \{p\boldsymbol{n} + \rho\boldsymbol{v}(\boldsymbol{v}\cdot\boldsymbol{n})\}\, dS \tag{3}$$

The far-field expression for the lift can be written as an integral over the exit plane by moving the inlet and side planes to infinity:

$$L = -\int_{S_2} (\rho uw)\, dS \tag{4}$$

Application of the Stoke theorem allows us to write Eq. (4) in the following form:

$$L = \int_{S_2} [y\{\nabla \times (\rho u\boldsymbol{v})\}\cdot\boldsymbol{i}]\, dS \tag{5}$$

Noting that $\{\nabla \times (\rho u\boldsymbol{v})\}\cdot\boldsymbol{i} = \partial(\rho uw)/\partial y - \partial(\rho uv)/\partial z$ and introducing the perturbation velocity $u' = u - U_\infty$, eq. (5) can be written as

$$L = U_\infty \int_{S_2} \left[y \left\{ \frac{\partial(\rho w)}{\partial y} - \frac{\partial(\rho v)}{\partial z} \right\} \right] dS$$

$$+ \int_{S_2} \left[y \left\{ \frac{\partial(\rho u'w)}{\partial y} - \frac{\partial(\rho u'v)}{\partial z} \right\} \right] dS \tag{6}$$

The velocity perturbation u' has a nonzero value for S_2 to $x \to \infty$ (see Batchelor[5]) and, consequently, the second integral of Eq. (6) does not necessarily vanish in the limit. Although not zero, the contribution of this integral is small compared to the contribution of the first integral. Assuming incompressible flow and introducing the streamwise vorticity component $\xi = \partial w/\partial y - \partial v/\partial z$, Eq. (6) can be written in the form of a wake integral:

$$L = \rho_\infty U_\infty \int_{S_2} (y\xi)\, dS \tag{7}$$

The far-field expression for the drag can be rearranged in a similar manner as the far-field expression for the lift (assuming incompressible conditions):

$$D = \rho_\infty/2 \int_{S_2} \{(v^2 + w^2) - (u - U_\infty)^2\}\, dS \tag{8}$$

Maskell[6] and later Wu et al.[7] have shown how this integral can be converted into a wake integral by introducing the continuity equation

$$\frac{\partial v}{\partial y} + \frac{\partial w}{\partial z} = -\frac{\partial u}{\partial x} = f \tag{9}$$

the vorticity vector

$$\omega = i\xi + j\eta + k\omega = \nabla \times \boldsymbol{v} \tag{10}$$

and two scalar functions $\psi(y,z)$ and $\phi(y,z)$ such that

$$v = \frac{\partial \psi}{\partial z} + \frac{\partial \phi}{\partial y};\ w = -\frac{\partial \psi}{\partial y} + \frac{\partial \phi}{\partial z} \tag{11}$$

By substituting Eqs. (9–11) into Eq. (8) it can be shown that the expression for the drag becomes

$$D = \rho_\infty/2 \int_{S_2} \{\psi\xi - \phi f - (u - U_\infty)^2\}\, dS \tag{12}$$

where

$$\psi(y,z) = -1/(2\pi) \int_{S_2} [\xi(y^*,z^*) \ln\{(y^* - y)^2 + (z^* - z)^2\}^{0.5}]\, dS \tag{13}$$

$$\phi(y,z) = 1/(2\pi) \int_{S_2} [f(y^*,z^*) \ln\{(y^* - y)^2 + (z^* - z)^2\}^{0.5}]\, dS \tag{14}$$

In the limit as S_2 goes to $x \to \infty$ the variable f vanishes. However, the term $(u\text{-}U_\infty)^2$ retains an admittedly small, but finite value. In order to reduce Eq. (12) to a wake integral, this term is neglected and

$$D = \rho_\infty/2 \int_{S_2} (\psi\xi)\, dS \tag{15}$$

Three sets of equations for the calculation of the forces exerted on a wing from inviscid, incompressible flowfield solutions are obtained. Equation (3) represents the classical near-field and far-field expressions for the lift and the drag, and Eqs. (7) and (15) represent the wake-integral expressions for the two components of the total force.

Reference Test Case

The flow around a wing is studied at a Mach number of $M_\infty = 0.2$. The pertinent points of the wing planform are its unswept straight trailing edge, curved leading edge, and elliptic spanwise chord distribution $c(\eta) = c_r(1 - \eta^2)^{0.5}$ where c_r represents the root chord (reference length) and η denotes the nondimensional spanwise station $y/(b/2)$. Here, the reference chord length $c_r = 1.0$ and the semispan $b/2 = 2.749$ resulting in a wing aspect ratio $AR = b^2/S = 7.0$. At the tip this wing has zero chord length. To avoid numerical difficulties in this region the present wing is given a small but finite chord length at the tip $c_t = 0.05$ by terminating the span at $\eta = 0.9987$. Consequently, the wing has a true aspect ratio of AR = 6.982. The sectional shape of the wing in the freestream direction is provided by the slightly modified (sharp trailing edge) NACA-0012 airfoil.

According to lifting-line theory (e.g., Ref. 8), the above wing has an elliptic spanwise load distribution and the relationship between the (induced) drag coefficient and the lift coefficient is given by $C_D = K_i C_L^2/(\pi \cdot AR)$ with the induced efficiency $K_i = 1.0$. This result is not rigorously exact and several hypotheses are introduced to obtain $K_i = 1.0$.[8] One of these hypotheses stipulates that the vortex sheet that originates at the trailing edge of the wing does not deform downstream and remains flat. For the present test case the effects of this and other simplifications are small, i.e., $|1\text{-}K_i| < 0.05$, and the above expression gives a good approximation of the drag at inviscid, subsonic conditions.

The numerical grid generator developed by Barth et al.[9] is applied to generate a *C*-grid about the modified NACA-0012 airfoil at each spanwise wing station. A *C-H* grid topology is obtained by placing these planar two-dimensional *C*-grids adjacent to each other. The *C-H* grid topology is preferred over the *C-O* topology for the present problem with the very small

wing-tip chord and it facilitates the evaluation of the surface integrals in the force calculations. Most of the results presented in this paper are obtained for a "medium grid" that consists of ($c \times s \times n$) 121 × 51 × 40 points with a surface grid of ($c \times s$) 62 × 30 points (Fig. 1). To facilitate the postprocessing of the results, the grid system is generated for a specific angle of attack α. As a result, the α-input for the flow code is always zero and the freestream vector is always oriented in the positive x direction.

Results and Discussion

The results presented in this paper have been obtained with the LANS3D finite difference code developed by Obayashi et al.[10] The steady solution of the compressible Euler/Navier-Stokes equations is obtained by time integration in a time-asymptotic fashion. Both second- and fourth-order dissipation terms are added for numerical stability.

In addition to the solutions for the earlier discussed "medium grid," solutions for a "coarse grid" and a "fine grid" will be presented. The former grid consists of 121 × 41 × 25 = 124,025 points of which are 62 × 20 distributed on the wing surface, whereas the latter has 121 × 71 × 50 = 429,550 grid points including 62 × 45 points on the surface. Note that the grid is only refined in the spanwise and the normal directions, whereas it is kept constant in the streamwise direction. This results in a constant definition of the wing section shape and minimizes changes in the solution while refining the grid as a result of changes in the geometry of the wing.

In Fig. 2 the convergence characteristics for the wing at α = 2 deg and the medium grid are shown. Initially, the CFL number based on the smallest cell size is set to 5 with a corresponding time step of 0.05. Slowly the step size is increased until after about 5000 steps the solution is fully converged. At that point the CFL number has increased to 10^4 and the time step to 10. The second- and fourth-order dissipation terms are slowly decreased throughout the time-stepping process. For all three solutions (coarse, medium, and fine grid) the identical end values are used (0.25 for the second-order and 3.0 for the fourth-order term). In addition to the wake-integrated values for the lift coefficient C_L and the drag coefficient C_D as obtained from Eqs. (7) and (15), respectively, C_L as obtained from surface-pressure integration is also plotted. In order to evaluate the wake integrals, a transverse plane at a specified location downstream of the configuration is selected and the two crossflow velocity components v and w are calculated on this plane through interpolation. Next, the streamwise vorticity component ξ and the stream function ψ are calculated. Initially, the wake-integrated value for C_L is lagging the surface-pressure value. However, once the solution approaches the steady (converged) condition, the values for C_L become nearly identical.

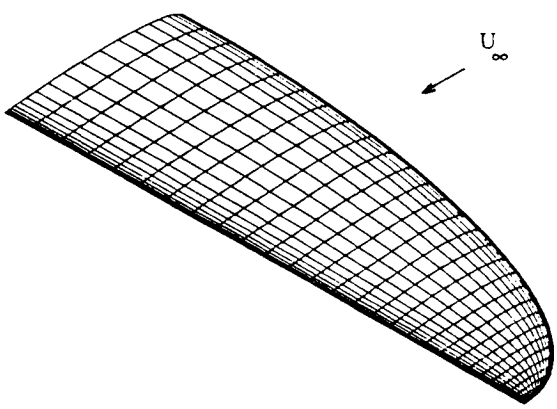

Fig. 1 Surface grid distribution for reference wing (medium grid).

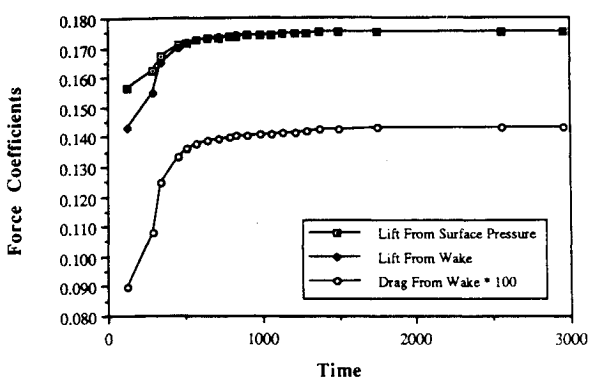

Fig. 2 Convergence history for lift coefficient and drag coefficient at α = 2 deg (medium grid).

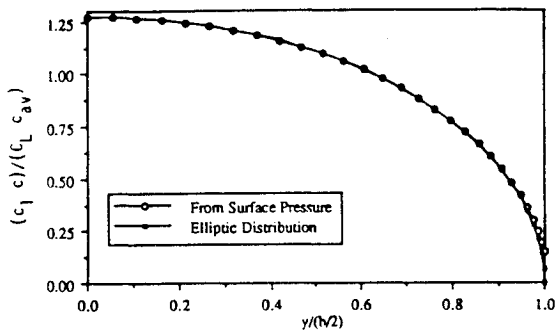

Fig. 3 Spanwise load distribution obtained from surface pressure integration at α = 4 deg (medium grid).

In Fig. 3 the spanwise load distribution $(c_l c)/(C_L\ c_{av})$ as obtained from the integration of surface pressures is plotted and compared with the elliptic load distribution. Here, c_l denotes the sectional lift coefficient and $c_{av} = S/b$ is the average chord. The computed distribution agrees quite well with the elliptic distribution and, consequently, the induced efficiency K_i is expected to have a value close to unity for this wing with attached flows.

In Table 1 the results for the three force-prediction techniques are summarized for α = 2 deg and α = 4 deg. Here, the wake-integration technique is applied at several transverse planes where Δx represents the distance of the plane downstream from the wing trailing edge. The lift prediction is shown to be nearly independent of the calculation technique. It should be noted, however, that application of the momentum-integration technique tends to result in less accurate force predictions when the integration domain is enlarged. This degradation in the accuracy of the force prediction can be attributed to the increase in the truncation error and the error introduced by the numerical viscosity with increasing distance from the body (i.e., increasing grid size), and the proximity of the approximate far-field boundary condition.[4,11] For C_L = 0.350 (C_L = 0.175) and K_i = 1.0, the drag coefficient should be C_D = 0.0056 (C_D = 0.0014). The results in Table 1 indicate that only the wake integration gives drag values that are close to these values, whereas the surface-pressure integration and the far-field momentum integration produce incorrect values for the drag. The inherent numerical viscosity in Euler solutions is the main source of this error in the drag prediction. The wake-integration technique allows us to circumvent the detrimental effect of the numerical viscosity on the drag prediction.

The predicted lift coefficient as obtained from surface pressure integration is nearly identical for all three grids (see Table 1). However, the drag coefficient based on the integration of the surface pressures varies somewhat with grid density with the fine-grid solution showing the least error. The fine-grid solution also provides more accurate drag values when the momentum-integration technique is applied, proving that the truncation error contributes significantly to the force-prediction problems encountered with this technique. For all three grids, the wake-integration technique gives the most accurate and consistent results.

Table 1 Lift coefficients and drag coefficients obtained with various force calculation techniques

Force analysis technique	Medium grid α = 2 deg		Medium grid α = 4 deg		Fine grid α = 4 deg		Coarse grid α = 4 deg	
	C_L	C_D	C_L	C_D	C_L	C_D	C_L	C_D
Surface pressure integ.	0.1751	0.0032	0.3496	0.0081	0.3482	0.0080	0.3496	0.0086
Far-field integration	0.1750	0.0026	0.3496	0.0079	0.3481	0.0075	0.3493	0.0079
Wake integration								
$\Delta x/c_r$ = 0.1	0.1754	0.0014	0.3498	0.0057	0.3486	0.0056	0.3491	0.0056
$\Delta x/c_r$ = 0.5	0.1760	0.0014	0.3510	0.0056	0.3485	0.0054	0.3487	0.0053
$\Delta x/c_r$ = 1.0	0.1763	0.0014	0.3509	0.0054	0.3493	0.0053	0.3485	0.0052

Conclusions

Several techniques for the calculation of drag using an Euler-equation formulation are discussed and compared. The technique based on the integration of the surface pressures (near-field) and two far-field techniques, one based on the integration of the momentum flux along a closed contour enclosing the configuration and the second based on the evaluation of a wake integral, are described and applied to three-dimensional flowfield solutions. The present calculations are limited to steady, low-Mach-number flows in the absence of active systems such as surface blowing/suction and propulsion.

The far-field technique based on the wake of the wing appears to provide the most consistent and accurate drag predictions. Both the surface pressure integration technique and the momentum-integration technique give erroneous drag values, mainly as a result of the inherent numerical viscosity in the Euler solutions and the inadequate grid resolution in the flowfield.

Acknowledgment

This work was supported by the NASA Ames Research Center under the Joint Research Interchange NCA2-397.

References

[1]van Dam, C. P., Nikfetrat, K., Vijgen, P. M. H. W., and Fremaux, C. M., "Calculation and Measurement of Induced Drag at Low Speeds," SAE Paper 901035, Oct. 1990.

[2]Slooff, J. W., et al., "Technical Status Review on Drag Prediction and Analysis from Computational Fluid Dynamics: State of the Art," AGARD Advisory Rept. 256, June 1989.

[3]Hicks, R. M., et al., "Euler and Potential Computational Results for Selected Aerodynamic Configurations," *Applied Computational Aerodynamics*, edited by P. A. Henne, Vol. 125, Progress in Astronautics and Aeronautics, AIAA, New York, 1990, pp. 263–385.

[4]Yu, N. J., Chen, H. C., Samant, S. S., and Rubbert, P. E., "Inviscid Drag Calculations for Transonic Flows," AIAA Paper 83-1928, July 1983.

[5]Batchelor, G. K., "Axial Flow in Trailing Line Vortices," *Journal of Fluid Mechanics*, Vol. 20, Pt. 4, 1964, pp. 645–658.

[6]Maskell, E. C., "Progress Towards a Method for the Measurement of the Components of the Drag of a Wing of Finite Span," RAE Technical Rept. 72232, Dec. 1972.

[7]Wu, J. C., Hackett, J. E., and Lilley, D. E., "A Generalized Wake-Integral Approach for Drag Determination in Three-Dimensional Flows," AIAA Paper 79-0279, Jan. 1979.

[8]Milne-Thomson, L., *Theoretical Aerodynamics*, 4th ed., Dover, New York, 1973.

[9]Barth, T. J., Pulliam, T. H., and Buning, P. G., "Navier-Stokes Computations for Exotic Airfoils," AIAA Paper 85-0109, Jan. 1985.

[10]Obayashi, S., Fujii, K., and Gavali, S., "Navier-Stokes Simulation of Wind-Tunnel Flow Using LU-ADI Factorization Algorithm," NASA TM 100042, Feb. 1988.

[11]Paisley, M. F., and Hall, M. G., "Improvements in the Formulation and Numerical Solution of the Euler Problem for Swept Wings," *Symposium Transsonicum III*, edited by J. Zierep and H. Oertel, Springer, New York, 1989, pp. 87–96.

Technical Comments

Comment on "Transition Effects on Airfoil Dynamics and Implications for Subscale Tests"

D. G. Mabey* and P. R. Ashill*
Royal Aerospace Establishment, Bedford MK41 6AE, England, United Kingdom

In Ref. 1, L. E. Ericsson repeats flawed explanations[2] for the results of our previous observations,[3] which we have already rebutted.[4] However, we regret that a further rebuttal is necessary because in Ref. 1 Ericsson has misinterpreted an unpublished report that is not widely available.[5]

Reference 5 provided small sketches of p/pt (where p and pt are the static and total pressure, respectively) that were intended merely to represent the general character of the wing pressure distributions. Ericsson has reproduced these, labeled as curves of $-Cp$, and made some unrealistic inferences. We offer the following brief remarks:

1) With regard to the measurements at M = 0.80, R = 6.5 × 10^6 (Ref. 1, Fig. 11), the milder adverse pressure gradient with the RAE 5237 profile compared to the RAE 5238 ensures that the growth of the boundary layer over the rear of the aerofoil is less rapid for the former than for the latter. Hence, the response for the RAE 5237 profile is smaller, as explained in Ref. 3.

2) With regard to the comparison of measurements at M = 0.5 and 0.8 on RAE profile 5238 (Ref. 1, Fig. 12 and Fig. 1 here based on the measurements of Ref. 5), the larger response at M = 0.5 is due, primarily, to the larger induced incidence (due to the decreased freestream velocity) compared to M = 0.80. It is likely that the differences in the C_p distribution, Reynolds number, and aerodynamic damping do not contribute significantly to the widely differing responses.

3) With regard to the comparison of measurements at M = 0.8 on RAE profile 5238 at two Reynolds number (Ref. 1, Fig. 13), the response is higher at R = 6.5 × 10^6 than at 3.0 × 10^6 primarily because of the increased magnitude of the negative aerodynamic damping (proportional to the product of density × velocity). Ericsson cannot justify his remark

Received May 24, 1990; accepted for publication Jan. 7, 1991.

*Senior Principal Scientific Officer.